Inductively coupled nonthermal plasma synthesis of aluminum nanoparticles

IOP Publishing Nanotechnology
Nanotechnology 32 (2021) 395601 (11pp) https://doi.org/10.1088/1361-6528/ac0cb3

Inductively coupled nonthermal plasma synthesis of aluminum nanoparticles

Chad A Beaudette[1], Himashi P Andaraarachchi[1], Chi-Chin Wu[2] and Uwe R Kortshagen[1]

[1] Department of Mechanical Engineering, University of Minnesota - Twin Cities, Minneapolis, Minnesota, United States of America
[2] Weapon Sciences Division, Weapons and Materials Research Directorate, US Army Combat Capabilities Development Command Army Research Laboratory, Aberdeen Proving Ground, Maryland, United States of America

E-mail: kortshagen@umn.edu

Received 11 April 2021, revised 10 June 2021
Accepted for publication 17 June 2021
Published 6 July 2021

Abstract

Metallic nanoparticles of aluminum (Al), a nontoxic and earth-abundant element, are relevant to plasmonic and energetic applications. However, monodisperse Al nanoparticles are difficult to synthesize using all gas-phase approaches, especially in the 10 to 20 nm size range; yet, many applications require particles of this size due to their enhanced properties. Here, an inductive nonthermal plasma reactor fed with aluminum trichloride ($AlCl_3$) and Ar is used to synthesize single-crystal aluminum nanoparticles. The particles can be produced with or without hydrogen. Several reactor conditions such as $AlCl_3$ vapor concentration, flow rates, and power are found to strongly influence particle properties such as the oxide shell thickness, particle mono-dispersity, and particle size. Significant quantities of Ar relative to $AlCl_3$, short residence times of 10 s of ms, and pressures in excess of 4.7 Torr are required to form Al particles with geometric mean sizes of 10–20 nm and geometric standard deviations as low as 1.3. While the Al nanoparticles are covered with 2–4 nm thick oxide shells, the best synthesis conditions yield particle sizes determined by electron microscopy that are comparable to crystallite sizes determined from x-ray diffraction.

Supplementary material for this article is available online

Keywords: nonthermal plasma, synthesis, nanoparticle, aluminum, vapor phase, aerosol

(Some figures may appear in colour only in the online journal)

1. Introduction

Due to their tendency to easily oxidize, metals are difficult to synthesize at the nanoscale but serve as a basis for many applications including catalysts [1–4], aluminum-based batteries [5, 6], energetics [7], biomedicine [8], metallic glasses [9], structural applications [10], and photonics [4, 11]. One such metal, aluminum (Al), is earth-abundant, nontoxic, and is utilized in lithium ion batteries [5], biomedical applications [12], energetic materials [13], hydrogen production [14], hydrogen storage [15], plasmonics and photonics [4, 16], and catalysis [1]. To optimize and enable some of these applications requires a reliable synthesis process for crystalline Al nanoparticles in the 10–20 nm size range with low polydispersity [17, 18].

Commercial Al is produced in sizes ranging from 40 nm to tens of micrometers [19, 20] using vapor phase nucleation, which results from physical supersaturation followed by condensation to form Al droplets. However, the synthesis of monodisperse Al nanoparticles is still elusive [20]. Current synthesis methods often suffer from broad particle size distributions, an inability to create particles of a specific diameter at the nanometer scale, contamination, and agglomeration issues [20]. The methods employed to produce nanoparticles of Al and other metals include electric explosion of wires [21], wet synthesis routes [22–25], plasma synthesis via

thermal [26] and nonthermal [27] plasmas, vapor-condensation [28–30], flame synthesis [31], mechanical milling of large metal particles [32, 33], and laser ablation [34–36]. However, many of these synthesis methods lack control over particle size and size distribution and some are not compatible with the integrated growth of a shell material that could protect the metal nanoparticles from oxidation.

Nonthermal plasmas can generate radical species at low temperatures that otherwise could not be generated without excessive heat. The result is a highly reactive electro-chemical environment that has been utilized in the synthesis of a large class of nanomaterials that includes many elemental nanoparticles [37–51], particles of doped semiconductors [52, 53], particles that were coated with ligands in an integrated all-gas-phase process [54–56], and nanocomposites [40–42, 57, 58]. To date, nonthermal plasmas have been scantly applied to the synthesis of metal nanoparticles, and carbon contamination from the metal organic precursors was found to be a major problem [49–51]. However, devising nonthermal plasma processes for the synthesis of high purity nanoparticles is very appealing because nonthermal plasmas lend themselves to the facile integration with inorganic shell growth processes to form core–shell nanoparticles [45, 46, 56]. Shells may be designed to protect nanoparticle cores from oxidation and other environmental influences.

In this paper, we focus on the synthesis of Al nanoparticles from an aluminum containing chloride precursor rather than a metal organic precursor where carbon contamination would be difficult to avoid [59]. Specifically, we investigate the synthesis of Al nanoparticles from aluminum trichloride ($AlCl_3$) in a single-step gas phase process, which has to date not been demonstrated. Chlorinated precursors have previously been used for the synthesis of group IV semiconductor nanoparticles [47, 48, 60, 61] where it was found that hydrogen is required as a scavenger for chlorine to enable the nucleation of nanoparticles. We demonstrate that Al nanoparticles can be produced with or without hydrogen, in contrast to previous reports on group IV particles [47, 48, 60, 61]. The effects of plasma power and gas flow rates will be discussed below. While an important and logical next step, the formation of core–shell particles to protect Al nanoparticles from environmental influences is not considered in this study.

2. Experimental methods

2.1. Precursor and process gas selection

The emphasis of this work is on the synthesis of Al nanoparticles with minimal amounts of impurities. For this reason, we did not select common metal organic precursors such as trimethyl aluminum or triethyl aluminum, which, in our preliminary, unpublished work, had led to significant carbon impurities. Instead, we decided on a chloride-based precursor, aluminum trichloride, $AlCl_3$, which is solid at room temperature but has a significant vapor pressure when heated.

Solid precursors are more difficult to work with than gaseous precursors because decomposition, condensation, and flow control are critical parameters that strongly effect nanoparticle synthesis. However, $AlCl_3$ has a significant vapor pressure at temperatures as low as 100 °C [62]. Contamination from Cl groups, which might appear to be a significant problem, has been shown to be mitigatable with or without hydrogen in other plasma-produced materials that have used chlorine-based precursors [39, 44, 63].

Traditional methods for nanoparticle synthesis rely on flow-through reactors where precursors are injected at the inlet side and flown through the reactor and the electrodes. This method, however, would lead to Al deposition on the walls of the reactor between the exciting electrodes which eventually would prevent power deposition into the plasma as the RF electric field can no longer penetrate into the gas due to electrostatic screening by the metal. To circumvent this issue, a nontraditional midstream injection method was utilized in this study, as shown in figure 1. The upstream Argon flow Ar_{up} forms a sheath flow around the $AlCl_3$ injector and limits deposition of an Al film on the reactor walls inside of the induction coil.

$AlCl_3$ was selected as a precursor because of its lack of any carbon-containing groups, its substantial vapor pressure at relatively low temperatures, and its well known pathways to the formation of Al films in electrolysis and plasma systems [64, 65]. Electrochemical pathways for Al film formation and decomposition of $AlCl_3$ are well studied and several pathways exist [64]. These pathways include both chemical supersaturation pathways such as $2AlCl_4^-(g) \rightarrow Al_2Cl_7^-(s) + Cl^-(g)$ and physical supersaturation pathways such as $AlCl_3(g) + 3e^- \rightarrow Al(s) + 3Cl^-(g)$. These mechanisms were also studied in an inductive discharge for Al film formation at a low pressure of 300 mTorr by Zheng *et al* [65]. The authors found that an increase in the ratio of Ar to $AlCl_3$ and H_2 resulted in more decomposition of $AlCl_3$ into AlCl and Al radicals compared to a plasma with H_2 only [65]. Interestingly, they reported no optical emission from Cl, but strong emission from AlCl, Al, and H atoms. This might elude to pathways where Cl_2 gas and HCl are the predominant byproducts of the reactions similar to those found by Ding *et al* for silicon nucleation from silane [60]. However, they also found that no Al metal film was formed when a plasma consisting of only $AlCl_3$ + Ar was used. This behavior is consistent with several other reports where authors were unable to obtain particles from chlorinated precursors without addition of hydrogen [47, 48, 60, 61].

Hydrogen is often used to scavenge chlorine gas to form HCl. Chlorine gas would otherwise react with Al, leading to etching of the formed particles within the discharge. The etch reaction, $2Al + 3Cl_2 \rightarrow 2AlCl_3$, proceeds at modest temperatures and depends on the formation rate of Cl_2 gas from anionic Cl that is released during particle nucleation. Hydrogen addition drives the reaction $2Al + 6HCl \leftrightarrow 2AlCl_3 + 3H_2$ to the left. Hence, one should expect that increasing the amount of H_2 should lead to less Cl_2 gas formation and Al particle formation should be more favorable [66]. The H_2 addition also decreases the barrier to the

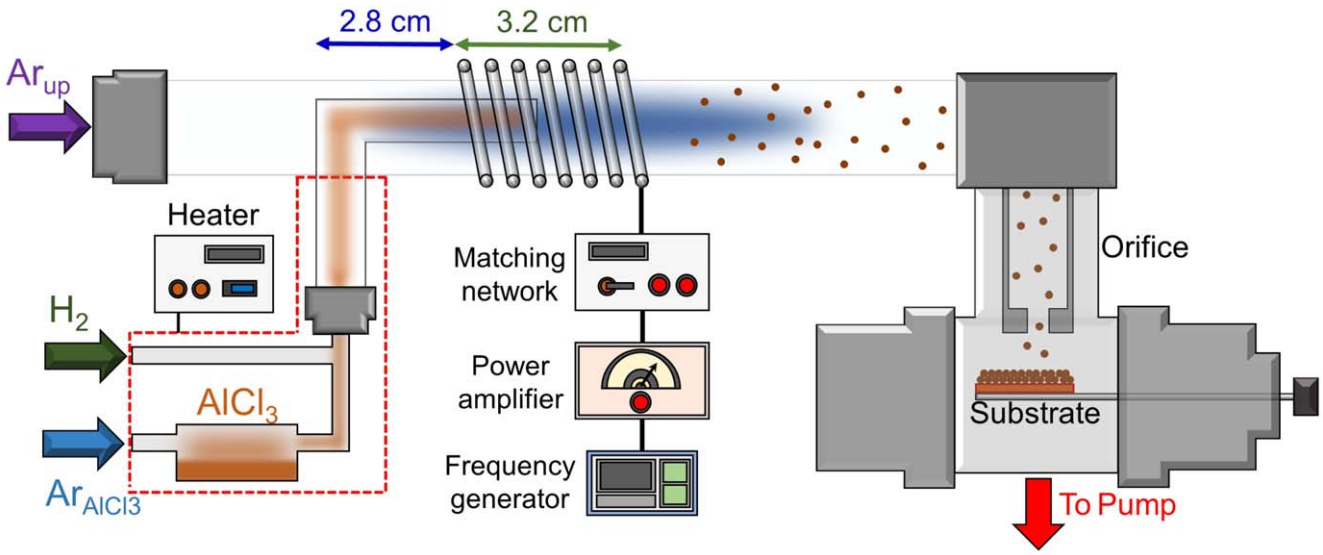

Figure 1. A schematic of the reactor used to produce Al nanoparticles. An inductive discharge is excited via a radiofrequency power supply that is coupled to a seven turn copper induction coil via a matching network. $AlCl_3$ is sublimated via a heating tape; heated reactor sections are shown with a dashed red line. A downstream orifice is used to maintain the pressure upstream and impact the particles onto a moving substrate for collection and analysis.

breakdown of $AlCl_3$ which further improves the kinetics in the plasma [65].

2.2. Plasma synthesis conditions and reactor details

Al nanoparticles are formed in a nonthermal inductively coupled plasma (ICP) reactor, previously discussed in detail by Beaudette *et al* [63]. Briefly, the reactor is shown in figure 1 and utilizes a quartz tube with 355 mm length, 25 mm outer diameter, and 21.8 mm inner diameter as the reaction vessel. A radiofrequency (RF) electric field is induced by a 7 turn copper induction coil with a length of 3.2 cm whose upstream end is positioned 2.8 cm from the upstream end of the precursor injection port, figure 1. The $AlCl_3$ injection port is a 9.6 mm outer diameter quartz tube (standard 3/8 inch ultratorr dimension) with a 7 mm inner diameter that is 51 mm in length. The distance between the $AlCl_3$ injection port and the upstream argon inlet, Ar_{up}, injection port is 127 mm. An ICP is excited and maintained by a 13.56 MHz RF signal with nominal powers between 80 and 235 W. The RF power is generated by a Tektronix AFG 3251 arbitrary function generator that creates a driving signal with a peak-to-peak voltage between 0.6 and 1.8 Vpp which is fed into an ENI A150-1210 power amplifier (55 db gain) and then into a Vectronics HFT1500 matching network. Reported powers within the figures reflect the output power of the amplifier. The actual power coupled into the plasma is expected to be lower due to losses in the RF components. Except when the effect of discharge power is studied, the power is kept at 80 W.

Argon is flown from upstream of the injection port (Ar_{up}) at a flow rate that is varied between 185 and 425 standard cubic centimeter per minute (sccm). The hydrogen flow was varied between 0 and 30 sccm. For each reactor run, 2.5 g of fresh $AlCl_3$ (Sigma Aldrich 99.99% Metals basis) precursor were added to a sublimator, which was then heated using BriskHeat heating tape (BWH051040L) and an Applied Thermal Systems controller. The heated sections of the reactor are highlighted by dashed red lines in figure 1 and are heated to 110 °C. Argon (Ar_{AlCl_3}) was flown through the sublimator at rates between 25 and 100 sccm to carry the $AlCl_3$ vapor into the reactor. Prior to establishing vapor flow from the $AlCl_3$ sublimator, the sublimator was heated for 10 min and an ICP was excited for 5 min to enable sufficient heating of the discharge chamber; temperature measurements of the reactor are reported elsewhere [63]. An orifice with opening dimensions of 4.5 mm × 0.7 mm and thickness of 10 mm was used to control the upstream pressure and accelerate the flow and the entrained nanoparticles for impaction on the substrate [58]. Particles were impacted for 2 min per run for post processing at a downstream location located 38″ from the plasma where the particles were synthesized. Reactions were carried out at various pressures between 3.8 and 5.3 Torr depending on the flow rates. The influence of discharge power was studied at 4.3 Torr (without hydrogen) and 4.7 Torr (with hydrogen). Downstream pressures were between 0.5 and 0.7 Torr.

The flow rate of $AlCl_3$ was estimated to be approximately 540 $\mu g\ s^{-1}$ based on the starting and ending quantity of $AlCl_3$ after 30 min of synthesis at a flow rate of 100 sccm of Ar_{AlCl_3}. During this period, the mass of $AlCl_3$ in the sublimator decreases from 2.5 to 1.5 g. The corresponding mass flow rate of $AlCl_3$ of 540 $\mu g\ s^{-1}$ translates into a partial pressure of $AlCl_3$ of 91 mTorr out of a total pressure of 4.7 Torr at a total argon flow rate of 285 sccm. The particle production rate is 10.2 $mg\ h^{-1}$ or 2.8 $\mu g\ s^{-1}$, resulting in a relatively poor precursor conversion rate of $<1\%$. We observed that $AlCl_3$ is lost primarily to the reactor walls in the form of an aluminum film and $AlCl_x$ species and to the pump as gaseous $AlCl_3$ fragments. Further research is needed in order to improve the precursor conversion to Al nanoparticles.

2.3. Materials characterization

X-ray photoelectron spectroscopy (XPS) was conducted on a PHI Versa Probe III XPS and UPS (UV Photoelectron Spectroscopy) system using an Al Kα source. A 55 eV band pass energy at a 100 μm spot size was used for high-resolution scans which were collected under neutralizing ion and electron irradiation (dual beam charge neutralization). An adventitious carbon signature located at 284.8 eV was used to fit the peaks. XPS survey scans were taken at a band pass energy of 280 eV for 5 scans in order to determine the chemical composition of the nanoparticle films which were then calculated using PHI's 'Multipak' software.

A Tecnai T12 transmission electron microscope (TEM) was used in bright field imaging mode at an accelerating voltage of 120 kV to determine particle sizes. More than 100 particles were measured in order to fit the log-normal size distributions and histograms shown in the figures with their accompanying geometric means (μ_g) and geometric standard deviations (σ_g). We used two different methods of TEM sample preparation. TEM samples in figure S1, available online at stacks.iop.org/NANO/32/395601/mmedia of nanoparticles produced at 25 and 50 sccm of Ar_{AlCl_3} with 30 sccm of H_2 and at 50 sccm Ar_{AlCl_3} samples with 0 sccm of H_2 were collected by direct impaction of the nanoparticles onto TEM grids after the slit orifice in a chamber about 38″ downstream of the plasma. These particles do not show agglomeration because they were collected directly from the gas phase post synthesis. All other TEM samples were collected by directly impacting the nanoparticles downstream of the slit orifice onto glass slides. These nanoparticle deposits were then scraped off and sonicated in ethanol for 2 min before drop casting them onto TEM grids. These samples do exhibit particle agglomeration, because they were collected as powders on a substrate, and capillary forces of the solvent used for drop casting also lead to agglomeration during solvent evaporation. X-ray diffraction (XRD) patterns were collected on a Bruker D8 Discover diffractometer that uses a beryllium 2D area detector and a Co Kα source. The patterns were then converted to Cu Kα patterns via the computing software Jade. Scans were collected on amorphous SiO_2; the broad amorphous background from SiO_2 was subtracted from the raw signal to get the final signal. XRD (111) Al peaks were fitted to determine approximate crystallite sizes using the Scherrer equation [67]; instrument broadening was accounted for using a LaB_6 standard.

3. Results and discussion

Our studies revealed that several parameters strongly control the overall production and yields of Al nanoparticles. The flow rates of Ar_{up} and Ar_{AlCl_3}, and plasma power were found to have significant effects on the particle production. Low vapor pressures of $AlCl_3$ caused by sublimator temperatures that were lower than 110 °C were insufficient for producing Al nanoparticles without hydrogen, and production rates with hydrogen were exceptionally weak at even 109 °C. High upstream flow rates Ar_{up} at or above 185 sccm were essential to Al particle production. Below we will discuss the effects of the flow rates and plasma power for Al particle production.

3.1. Effect of Ar_{AlCl_3} *flow rate*

To study the effect of argon flow through the sublimator, Ar_{AlCl_3}, the upstream flow rate of argon, Ar_{up}, was held constant 185 sccm. As Ar_{AlCl_3} was increased from 25 to 100 sccm the geometric mean of the particle size distributions was found to decrease when hydrogen was added, but did not change significantly when hydrogen was not added. Hydrogen within the discharge can react with chlorine to form HCl which has a lower etch rate for Al than Cl_2, Cl, or other Cl radicals [68]. Moreover, new chemical pathways for particle formation exist with hydrogen through decomposition and direct reactions with $AlCl_3$ to form intermediate radicals such as AlCl and $AlCl_2$ that would otherwise need to be created by electron collisions with the high energy $AlCl_3$ bonds [65, 69]. Particle formation can occur at lower input powers with hydrogen which, in turn, can lead to larger particles when compared to conditions without hydrogen as plasma electrons are not solely responsible for the decomposition of $AlCl_3$ and because Cl_2 discharges tend to have lower electron densities than HCl discharges [70], as shown in figures 2(a), (e) and S1. We note that the geometric standard deviation of 1.6–1.7 is larger than those that are typically observed in plasma synthesis of nanoparticles [71, 72]. The reason for this relatively broad size distribution is currently not understood and requires further study. Possible mechanisms leading to the broad size distribution could include agglomeration of neutral Al particles outside of the plasma or radial gradients in the precursor density due to the central injection of the Al precursor.

XPS scans of the produced nanoparticle films are shown in figures 2(c), (d) with hydrogen and in figures 2(g), (h) without hydrogen. The nanoparticle surfaces were irradiated with an argon ion beam within the XPS instrument for 1 min to remove surface contamination and the surface oxide layer. High resolution scans of the Al 2p peaks were taken and two significant peaks were found: one located at approximately 71 eV corresponding to metallic Al and the second at approximately 75 eV corresponding to aluminum oxide [73–76]. Particles produced without hydrogen had significantly larger Al fractions, between 28% and 34%, compared to samples produced with hydrogen, 18%–27%, suggesting a thicker oxide shell, although uneven etching of the nanoparticle films by the sputter source may be a factor too. Chlorine in the as-produced films was slightly lower for nanoparticles produced without hydrogen, at 3.8%–5.1%, than for particles produced with hydrogen, at 4.8%–5.8%. The small difference in chlorine concentration in the Al nanoparticles produced with and without hydrogen suggests that the Al particle nucleation from $AlCl_3$ in the plasma is more dependent on plasma electrons than on the presence of hydrogen.

The crystallite size, as determined by applying the Scherrer equation to the XRD measurements, is significantly

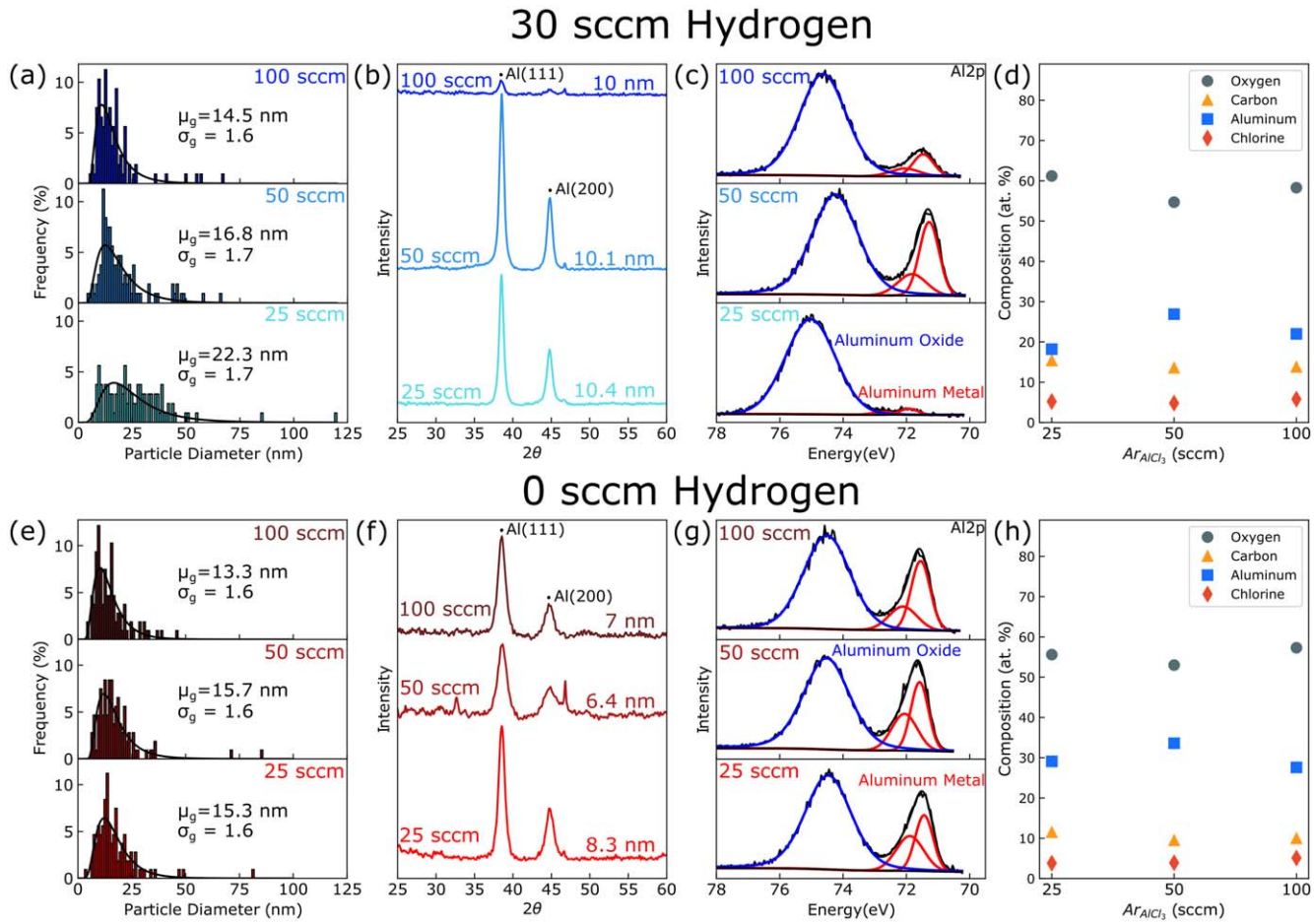

Figure 2. Particle size distributions from TEM analysis, XPS, and XRD of particles produced with Ar_{AlCl_3} flow rates between 25 and 100 sccm, Ar_{up} flow rate of 185 sccm, at 80 W of power (a)–(d) with 30 sccm of hydrogen and (e)–(h) without hydrogen. Particle size distributions with (a) 30 sccm of hydrogen and (e) without hydrogen. XRD for particles produced (b) with 30 sccm of hydrogen and (f) without hydrogen, particle sizes calculated from the Scherrer equation shown above each line. Al 2p high-resolution XPS scans of the particles produced (c) with 30 sccm of hydrogen and (g) without hydrogen. XPS Survey scans for particles produced (d) with 30 sccm of hydrogen and (h) without hydrogen.

smaller than the particle size measured by TEM, as shown by comparing the particle size distributions from TEM in figures 2(a), (e), with XRD scans in figures 2(b), (f) [67]. The XRD peaks represent cubic Al and were found to agree with literature [65, 77–79]. The discrepancy between the XRD crystallite size and TEM particle size, which is as large as 12 nm when the flow rate of Ar_{AlCl_3} was 25 sccm with hydrogen, might indicate condensation of excess $AlCl_3$ or its fragments onto the surface of the particles. When removed from the reactor and exposed to air, these $AlCl_x$ groups react with water vapor in the atmosphere to form an oxide layer. To counteract this effect, higher flow rates of Ar_{AlCl_3} of 100 sccm were used for the remaining experiments which led to significantly smaller particle sizes inferred from TEM imaging, a lower fraction of very large particles, and reduced $AlCl_3$ condensation downstream of the plasma than at Ar_{AlCl_3} flow rates of 25 or 50 sccm. The higher flow rate of Ar_{AlCl_3} of 100 sccm results in a lower gas phase concentration of $AlCl_3$ relative to argon and shorter residence times compared to the 25 and 50 sccm cases. These two factors reduce the overall growth of Al particles by $AlCl_x$ additions or by $AlCl_3$ condensation downstream of the plasma.

3.2. Effect of Ar_{up} flow rate

In order to decrease the vapor phase concentration of $AlCl_3$ in the gas phase and reduce the residence time of the gas in the plasma further, the flow rate of Ar_{up} was changed from 185 to 435 sccm while the Ar_{AlCl_3} flow rate was held constant at 100 sccm. The residence time of the particles in the plasma is shown in figure S2 and corresponds to roughly 13 ms for an Ar_{up} flow rate of 185 sccm case (315 sccm of total flow) and 8 ms for an Ar_{up} flow rate of 425 sccm case (565 sccm of total flow). This increase in flow rate caused the pressure in the reactor to change between 4.7 Torr (185 sccm), 5.0 Torr (325 sccm), and 5.3 Torr (435 sccm) when hydrogen was added and between 4.3 Torr (185 sccm), 4.7 Torr (325 sccm), and 5.0 Torr (435 sccm) when no hydrogen was added. The gas phase concentration of $AlCl_3$ relative to Ar at 285 sccm of total Ar flow ($Ar_{up} + Ar_{AlCl_3}$) is significantly higher than that at 535 sccm total Ar flow. Figure 3 shows the particle size

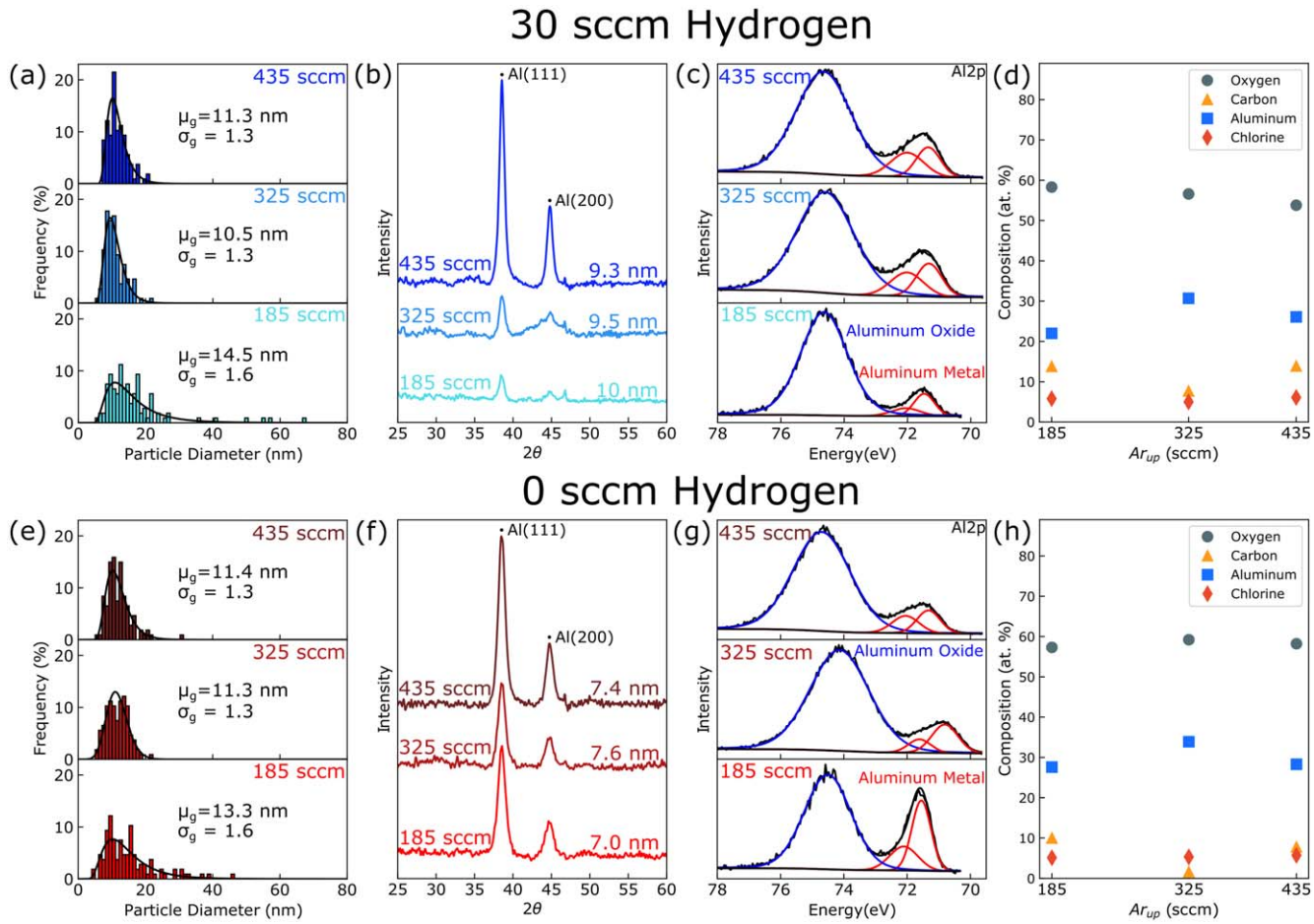

Figure 3. Particle size distributions from TEM analysis , XPS, and XRD of Al nanoparticles produced at 80 W of power with Ar_{up} flow rates between 185 and 435 sccm (a)–(d) with 30 sccm of hydrogen and (e)–(h) without hydrogen. Particle size distributions (a) with 30 sccm of hydrogen and (e) without hydrogen. XRD for particles produced (b) with 30 sccm of hydrogen and (f) without hydrogen, particle sizes calculated from the Scherrer equation shown above each line. Al 2p high-resolution XPS scans of the particles produced (c) with 30 sccm of hydrogen and (g) without hydrogen. XPS Survey scans for particles produced (d) with 30 sccm of hydrogen and (h) without hydrogen.

distributions determined by TEM, XRD, and XPS for particles produced by increasing the flow rate of the upstream argon (Ar_{up}) through the reactor. Sample TEM images of the particles are shown in figure 4. Particle agglomeration, visible in figure 4, is due to the collection method involving collection as powders and drop casting, as explained in the experimental section on TEM sample collection. Particle size distributions in figure 3(a) with hydrogen and 3(e) without hydrogen show that increasing the flow rate of argon, which subsequently dilutes the vapor of $AlCl_3$ in the gas phase, results in particles with geometric mean sizes between 10.5 and 11.5 nm, which are smaller than the particles produced previously at conditions of higher $AlCl_3$ concentrations. Additionally, the geometric standard deviation of these particles decreased from 1.6 to 1.3 as the total upstream argon flow rate was increased from 185 to 435 sccm, which also increased the pressure as discussed above. XRD of the particles shows crystallite sizes which decrease from 10 to 9.3 nm when pressure and flow rates were increased with hydrogen, figure 3(b). When hydrogen was not added, crystallite sizes ranged from 7 to 7.6 nm for the different flow rates, figure 3(f). Figure 3 also shows the XPS for Al particles produced with hydrogen (c), (d) and without hydrogen (g), (h) with chlorine contents that hover around 5%–6% for all produced samples regardless of hydrogen addition. Energy-dispersive x-ray spectroscopy scans for particle produced with the highest flow rate of Ar_{up} of 435 sccm with hydrogen showed trace amounts of chlorine, relative to aluminum and oxygen, figure S3. The strongest signature of elemental aluminum was observed for an Ar_{up} flow of 185 sccm without addition of hydrogen.

It is important to note that the shorter residence times and lower gas phase concentration of $AlCl_3$ caused by increasing Ar_{up} resulted in smaller particle sizes and geometric standard deviations from TEM analysis but did not significantly influence the overall crystallite sizes determined by XRD. We attribute this to a reduction in the AlCl fragments in the shell of the Al particles and a reduction in $AlCl_3$ condensation onto the particles. Additionally, the crystallite sizes were smaller for particles produced without hydrogen than with hydrogen in all cases, which we attribute to the increased etch rate of Al for Cl_2 gas compared to HCl.

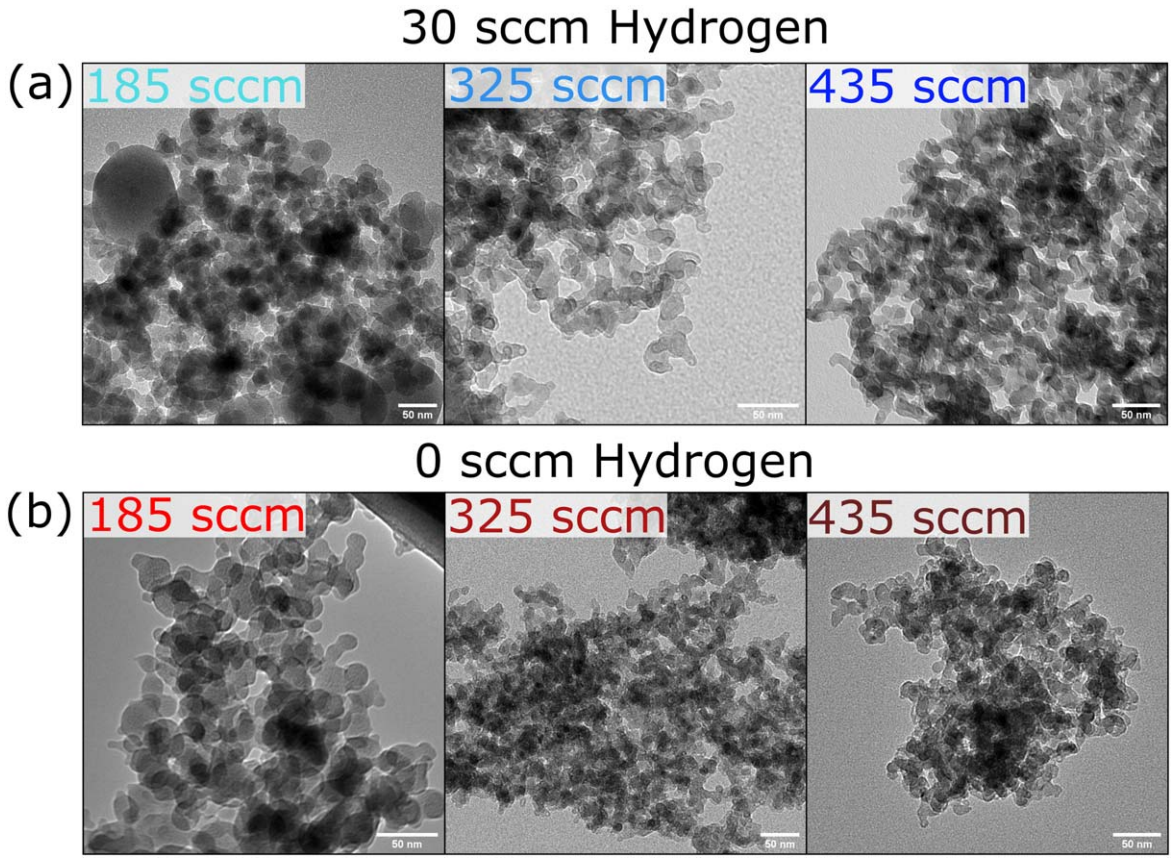

Figure 4. TEM of particles produced at 80 W of power with flow rates Ar_{up} between 185 and 435 sccm with (a) 30 sccm of hydrogen and (b) without hydrogen.

3.3. Effect of plasma power

The effect of the plasma input power was studied at constant conditions of 185 sccm of Ar_{up} because this was the minimum flow rate that was necessary to produce Al nanoparticles and 100 sccm of Ar_{AlCl_3} because it resulted in a lower quantity of larger nanoparticles in order to determine the role of increasing plasma density on the final Al particles. Hydrogen quenches the plasma by reducing the density of plasma electrons that are available for the direct decomposition of and reaction with $AlCl_3$ [65, 80, 81]. Higher powers in this case should be necessary to compensate for the reduction in electron density, to improve $AlCl_3$ vapor decomposition, and to form Al nanoparticles in the plasma. Particle size distributions in figure 5(a) with hydrogen and 5(b) without hydrogen show that increasing plasma power from 80 to 130 W decreases the geometric standard deviation of the particles from 1.6 to 1.3. The increased plasma density associated with increasing plasma power likely leads to more particle charging within the plasma and extends the afterglow region to further prevent agglomeration and favor monodisperse particle growth.

The geometric mean particle size was relatively unaffected by the power when hydrogen was added remaining between 14 and 15 nm. However, power significantly affected particle size when no hydrogen was added leading initially to a slight decrease in particle size from 13.3 to 12.4 nm when power was increased from 80 to 130 W and then to an increase in particle size to 17.4 nm when power was increased further to 185 W, as shown in figures 5(a), (e). TEM images of the particles are shown in figure S4. The mean size of the particles, as seen in figure 5(a), did not change while the crystallite sizes decreased from 10 to 7 nm, as inferred from Sherrer fits to the XRD data in figure 5(b), as power was increased from 80 to 235 W when hydrogen was added. This is due to a thicker oxide shell as indicated in the XPS scans by an increasingly weaker Al signal as the power is increased from 80 to 235 W, figure 5(c) [76]. A similar trend was also found when hydrogen was not added, figures 5(f), (h). Figure 5 also shows the elemental composition derived from XPS for Al particles produced (d) with hydrogen and (h) without hydrogen. Chlorine increases with increasing power from 5% at 130 W up to 9.2% at 235 W for the particles produced with hydrogen. When hydrogen was absent, chlorine concentration in the nanoparticle films increases slightly from 5.1% at 80 W to 8.6% at 235 W.

The increase in chlorine content, figures 5(d), (e), the decrease in the Al 2p signal in XPS, figures 5(c), (g), and the decrease in the XRD Al crystallite size, figures 5(b), (f), as plasma power is increased suggests that increases in plasma power mainly caused an increased $AlCl_x$ shell growth. This may be due to condensation/reaction of $AlCl_x$ downstream of the plasma rather than Al core growth.

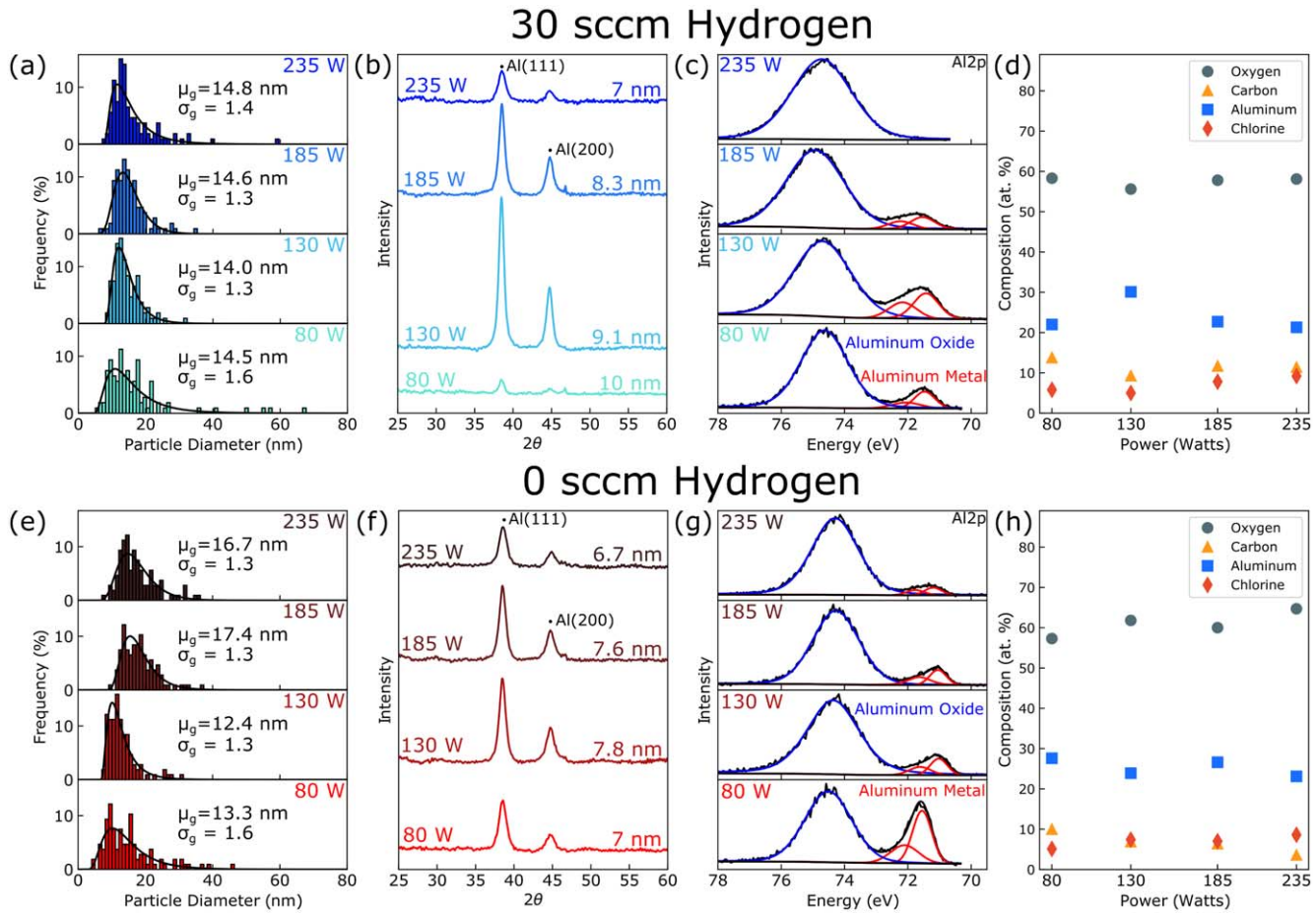

Figure 5. Particle size distributions from TEM analysis, XPS, and XRD of Al nanoparticles produced with powers between 80 and 235 W (a)–(d) with 30 sccm of hydrogen at 4.7 Torr and (e)–(h) without hydrogen at 4.3 Torr. Particle size distributions (a) with 30 sccm of hydrogen and (e) without hydrogen. XRD for particles produced (b) with 30 sccm of hydrogen and (f) without hydrogen, particle sizes calculated from the Scherrer equation shown above each line. Al 2p high-resolution XPS scans of the particles produced (c) with 30 sccm of hydrogen and (g) without hydrogen. XPS survey scans for particles produced (d) with 30 sccm of hydrogen and (h) without hydrogen.

4. Conclusions

Al nanoparticles were formed using a nonthermal inductive plasma utilizing $AlCl_3$ and Ar, both with and without hydrogen. It was found that parameters such as gas phase concentration of $AlCl_3$ and plasma power were critical to the formation of Al nanoparticles. Generally, hydrogen addition led to the formation of larger Al crystal core sizes compared to particles that were produced without hydrogen.

When flow rates of Ar_{AlCl_3} were increased from 25 to 100 sccm, leading to reduced $AlCl_3$/Ar concentrations, particle sizes decreased; particles were polydisperse in all cases with geometric standard deviations of 1.6–1.7, without and with hydrogen addition. Particles produced without hydrogen had lower chlorine content and higher Al content than particles produced with hydrogen. The significant differences between the geometric mean sizes determined by TEM and crystallite sizes measured by XRD indicated relatively thick oxide shells.

In order to obtain Al particles without significant oxide shell thicknesses relative to the core Al crystallite size, the flow rates of Ar_{up} through the plasma reactor were increased from 185 to 435 sccm. This resulted in the further dilution of the $AlCl_3$ vapor relative to the argon flow. This change produced particles of smaller sizes of ∼11 nm, with geometric standard deviations of 1.3. Crystallite sizes relative to the particle oxide shell thickness were significantly improved and resulted in crystallite sizes of 9.3 nm with hydrogen and 7.4 nm without hydrogen for particles of ∼11 nm in size at the highest total flow of Ar of 535 sccm (Ar_{up} + Ar_{AlCl_3}). It was also found that crystallite sizes were smaller for particles produced without hydrogen than with hydrogen in all cases, which is attributed to the increased etching rate of Al for Cl_2 gas compared to HCl.

Input plasma power was found to significantly influence the oxide layer thickness of the nanoparticles. Higher plasma power produced particles with smaller geometric standard deviations of 1.3 compared to particles produced at the lowest power with values of 1.6, which was linked to an increase in electron density. However, chlorine incorporation into the particles increased as a function of power, reaching 9.2% of the particle film composition at the highest power of 235 W even with hydrogen addition. Additionally, the fraction of Al metal relative to aluminum oxide increased with increasing power as crystallite size decreased. We suggest that this occurred due to increased radical densities of $AlCl_x$ species

which ultimately condensed and reacted with the Al particles to produce thicker shells of $AlCl_x$ as power was increased. Presumably, these thicker $AlCl_x$ shells reacted with water in the air to form thicker oxides.

At present, the conversion efficiency of $AlCl_3$ precursor into Al nanoparticles is still poor at below 1%. Future research will focus on improving this conversion efficiency.

Acknowledgments

This work was primarily supported by the US Army Combat Capabilities Development Command-Army Research Laboratory under Cooperative Agreement W911NF-19-2-0283. Part of this work was carried out in the College of Science and Engineering Characterization Facility, University of Minnesota, which has received capital equipment funding from the NSF through the UMN MRSEC program under Award DMR-2011401.

Data availability statement

The data that support the findings of this study are available upon reasonable request from the authors.

ORCID iDs

Chad A Beaudette https://orcid.org/0000-0002-5708-8133
Himashi P Andaraarachchi https://orcid.org/0000-0001-9736-1088
Chi-Chin Wu https://orcid.org/0000-0002-6036-3271
Uwe R Kortshagen https://orcid.org/0000-0001-5944-3656

References

[1] Hao Q, Wang C, Huang H, Li W, Du D, Han D, Qiu T and Chu P K 2015 Aluminum plasmonic photocatalysis *Sci. Rep.* **5** 15288
[2] Liu L, Zhang X, Yang L, Ren L, Wang D and Ye J 2017 Metal nanoparticles induced photocatalysis *Natl. Sci. Rev.* **4** 761–80
[3] Ahmad H, Kamarudin S, Minggu L and Kassim M 2015 Hydrogen from photo-catalytic water splitting process: a review *Renew. Sustain. Energy Rev.* **43** 599–610
[4] Swearer D F *et al* 2016 Heterometallic antenna-reactor complexes for photocatalysis *Proc. Natl. Acad. Sci.* **113** 8916–20
[5] Leisegang T, Meutzner F, Zschornak M, Münchgesang W, Schmid R, Nestler T, Eremin R A, Kabanov A A, Blatov V A and Meyer D C 2019 Aluminum-Ion battery: a sustainable and seminal concept? *Front. Chem.* **7** 1–21
[6] Das S K, Mahapatra S and Lahan H 2017 Aluminium-ion batteries: developments and challenges *J. Mater. Chem.* A **5** 6347–67
[7] Jena S and Gupta A 2019 *Nano-Energetic Materials for Defense Application* (Berlin: Springer) pp 81–108
[8] Zhang C, Yan L, Gu Z and Zhao Y 2019 Strategies based on metal-based nanoparticles for hypoxic-tumor radiotherapy *Chem. Sci.* **10** 6932–43
[9] Chen M 2011 A brief overview of bulk metallic glasses *NPG Asia Mater* **3** 82–90
[10] Wu G *et al* 2019 Hierarchical nanostructured aluminum alloy with ultrahigh strength and large plasticity *Nat. Commun.* **10** 5099
[11] Clavero C 2014 Plasmon-induced hot-electron generation at nanoparticle/metal-oxide interfaces for photovoltaic and photocatalytic devices *Nat. Photonics* **8** 95–103
[12] Park J 1991 *Concise Encyclopedia of Advanced Ceramic Materials* (Amsterdam: Elsevier) pp 13–6
[13] Jiang Y *et al* 2018 Energetic performance of optically activated aluminum/graphene oxide composites *ACS Nano* **12** 11366–75
[14] Roach P J, Woodward W H, Castleman A W, Reber A C and Khanna S N 2009 Complementary active sites cause size-selective reactivity of aluminum cluster anions with water *Science* **323** 492–5
[15] Graetz J, Reilly J, Yartys V, Maehlen J, Bulychev B, Antonov V, Tarasov B and Gabis I 2011 Aluminum hydride as a hydrogen and energy storage material: past, present and future *J. Alloys Compd.* **509** S517–28
[16] Knight M W, King N S, Liu L, Everitt H O, Nordlander P and Halas N J 2014 Aluminum for plasmonics *ACS Nano* **8** 834–40
[17] Huang Y, Risha G A, Yang V and Yetter R A 2009 Effect of particle size on combustion of aluminum particle dust in air *Combust. Flame* **156** 5–13
[18] Levitas V I, Asay B W, Son S F and Pantoya M 2007 Mechanochemical mechanism for fast reaction of metastable intermolecular composites based on dispersion of liquid metal *J. Appl. Phys.* **101** 083524
[19] Tsuzuki T 2009 Commercial scale production of inorganic nanoparticles *Int. J. Nanotechnol.* **6** 567
[20] Sundaram D, Yang V and Yetter R A 2017 Metal-based nanoenergetic materials: synthesis, properties, and applications *Prog. Energy Combust. Sci* **61** 293–365
[21] Kwon Y-S, Jung Y-H, Yavorovsky N, Illyn A and Kim J-S 2001 Ultra-fine powder by wire explosion method *Scr. Mater.* **44** 2247–51
[22] Meziani M J, Bunker C E, Lu F, Li H, Wang W, Guliants E A, Quinn R A and Sun Y-P 2009 Formation and properties of stabilized aluminum nanoparticles *ACS Appl. Mater. Interfaces* **1** 703–9
[23] Foley T J, Johnson C E and Higa K T 2005 Inhibition of oxide formation on aluminum nanoparticles by transition metal coating *Chem. Mater.* **17** 4086–91
[24] Cui Y, Huang D, Li Y, Huang W, Liang Z, Xu Z and Zhao S 2015 Aluminium nanoparticles synthesized by a novel wet chemical method and used to enhance the performance of polymer solar cells by the plasmonic effect *J. Mater. Chem.* C **3** 4099–103
[25] Fernando K A S, Smith M J, Harruff B A, Lewis W K, Guliants E A and Bunker C E 2009 Sonochemically assisted thermal decomposition of alane N,N -dimethylethylamine with titanium (IV) isopropoxide in the presence of oleic acid to yield air-stable and size-selective aluminum core-shell nanoparticles *J. Phys. Chem.* C **113** 500–3
[26] Bing Z 2007 Thermal plasma synthesis and photoinduced coating of aluminum nanoparticles *PhD Thesis* University of Minnesota Twin Cities
[27] Pearce B 2017 Nonthermal plasma synthesis of aluminum nanoparticles *Masters Thesis* University of Minnesota
[28] Panda S and Pratsinis S 1995 Modeling the synthesis of aluminum particles by evaporation-condensation in an aerosol flow reactor *Nanostruct. Mater.* **5** 755–67
[29] Schefflan R, Kovenklioglu S, Kalyon D, Mezger M and Leng M 2006 Formation of aluminum nanoparticles upon

condensation from vapor phase for energetic applications *J. Energy Mater.* **24** 141–56
[30] Suryanarayana C and Prabhu B 2007 *Nanostructured Mater* (Amsterdam: Elsevier) pp 47–90
[31] Calcote H and Felder W 1992 A new gas-phase combustion synthesis process for pure metals, alloys, and ceramics *Symp. Combust.* **24** 1869–76
[32] Jiang A, Wang F, Xia D, Li M, Qiang L, Zhu Z, Wang P, Fan R, Lin K and Yang Y 2019 Aluminum nanoparticles manufactured using a ball-milling method with ammonium chloride as a grinding aid: achieving energy release at low temperature *New J. Chem.* **43** 1851–6
[33] Eckert J, Holzer J, Ahn C, Fu Z and Johnson W 1993 Melting behavior of nanocrystalline aluminum powders *Nanostruct. Mater.* **2** 407–13
[34] Baladi A and Sarraf Mamoory R 2010 Investigation of different liquid media and ablation times on pulsed laser ablation synthesis of aluminum nanoparticles *Appl. Surf. Sci.* **256** 7559–64
[35] Stratakis E, Barberoglou M, Fotakis C, Viau G, Garcia C and Shafeev G A 2009 Generation of Al nanoparticles via ablation of bulk Al in liquids with short laser pulses *Opt. Express* **17** 12650
[36] Davari S A, Gottfried J L, Liu C, Ribeiro E L, Duscher G and Mukherjee D 2019 Graphitic coated Al nanoparticles manufactured as superior energetic materials via laser ablation synthesis in organic solvents *Appl. Surf. Sci.* **473** 156–63
[37] Mangolini L, Thimsen E and Kortshagen U 2005 High-yield plasma synthesis of luminescent silicon nanocrystals *Nano Lett.* **5** 655–9
[38] Schramke K S, Qin Y, Held J T, Mkhoyan K A and Kortshagen U R 2018 Nonthermal plasma synthesis of titanium nitride nanocrystals with plasmon resonances at near-infrared wavelengths relevant to photothermal therapy *ACS Appl. Nano Mater.* **1** 2869–76
[39] Alvarez Barragan A, Ilawe N V, Zhong L, Wong B M and Mangolini L 2017 A non-thermal plasma route to plasmonic TiN nanoparticles *J. Phys. Chem.* C **121** 2316–22
[40] Greenberg B L, Robinson Z L, Reich K V, Gorynski C, Voigt B N, Francis L F, Shklovskii B I, Aydil E S and Kortshagen U R 2017 ZnO nanocrystal networks near the insulator-metal transition: tuning contact radius and electron density with intense pulsed light *Nano Lett.* **17** 4634–42
[41] Greenberg B L, Ganguly S, Held J T, Kramer N J, Mkhoyan K A, Aydil E S and Kortshagen U R 2015 Nonequilibrium-plasma-synthesized ZnO nanocrystals with plasmon resonance tunable via al doping and quantum confinement *Nano Lett.* **15** 8162–9
[42] Thimsen E, Johnson M, Zhang X, Wagner A J, Mkhoyan K A, Kortshagen U R and Aydil E S 2014 High electron mobility in thin films formed via supersonic impact deposition of nanocrystals synthesized in nonthermal plasmas *Nat. Commun.* **5** 5822
[43] Felbier P, Yang J, Theis J, Liptak R W, Wagner A, Lorke A, Bacher G and Kortshagen U 2014 Highly luminescent ZnO quantum dots made in a nonthermal plasma *Adv. Funct. Mater.* **24** 1988–93
[44] Exarhos S, Alvarez-Barragan A, Aytan E, Balandin A A and Mangolini L 2018 Plasmonic core-shell zirconium nitride-silicon oxynitride nanoparticles *ACS Energy Lett.* **3** 2349–56
[45] Coleman D, Lopez T, Yasar-Inceoglu O and Mangolini L 2015 Hollow silicon carbide nanoparticles from a non-thermal plasma process *J. Appl. Phys.* **117** 193301
[46] Coleman D and Mangolini L 2019 Plasmonic core-shell silicon carbide-graphene nanoparticles *ACS Omega* **4** 10089–93
[47] Gresback R, Nozaki T and Okazaki K 2011 Synthesis and oxidation of luminescent silicon nanocrystals from silicon tetrachloride by very high frequency nonthermal plasma *Nanotechnology* **22** 305605
[48] Ahadi A M, Hunter K I, Kramer N J, Strunskus T, Kersten H, Faupel F and Kortshagen U R 2016 Controlled synthesis of germanium nanoparticles by nonthermal plasmas *Appl. Phys. Lett.* **108** 093105
[49] Woodard A, Xu L, Barragan A A, Nava G, Wong B M and Mangolini L 2018 On the non-thermal plasma synthesis of nickel nanoparticles *Plasma Process. Polym.* **15** 1700104
[50] Chiang W-H and Sankaran R M 2007 Microplasma synthesis of metal nanoparticles for gas-phase studies of catalyzed carbon nanotube growth *Appl. Phys. Lett.* **91** 121503
[51] Uner N B and Thimsen E 2017 In-flight size focusing of aerosols by a low temperature plasma *J. Phys. Chem.* C **121** 12936–44
[52] Rowe D J, Jeong J S, Mkhoyan K A and Kortshagen U R 2013 Phosphorus-doped silicon nanocrystals exhibiting mid-infrared localized surface plasmon resonance *Nano Lett.* **13** 1317–22
[53] Kramer N J, Schramke K S and Kortshagen U R 2015 Plasmonic properties of silicon nanocrystals doped with boron and phosphorus *Nano Lett.* **15** 5597–603
[54] Li Z and Kortshagen U R 2019 Aerosol-phase synthesis and processing of luminescent silicon nanocrystals *Chem. Mater.* **31** 8451–8
[55] Mangolini L and Kortshagen U 2007 Plasma-assisted synthesis of silicon nanocrystal inks *Adv. Mater.* **19** 2513–9
[56] Hunter K I, Held J T, Mkhoyan K A and Kortshagen U R 2017 Nonthermal plasma synthesis of core/shell quantum dots: strained Ge/Si nanocrystals *ACS Appl. Mater. Interfaces* **9** 8263–70
[57] Greenberg B L, Robinson Z L, Ayino Y, Held J T, Peterson T A, Mkhoyan K A, Pribiag V S, Aydil E S and Kortshagen U R 2019 Metal-insulator transition in a semiconductor nanocrystal network *Sci. Adv.* **5** eaaw1462
[58] Holman Z C and Kortshagen U R 2010 A flexible method for depositing dense nanocrystal thin films: impaction of germanium nanocrystals *Nanotechnology* **21** 335302
[59] Beaudette C A, Hunter K I, Kortshagen U R and Wu C-C 2020 Nonthermal plasma synthesis of aluminum nanoparticles from trimethyl aluminum *Army Res. Lab* **2020** 1–14 ARL-TR-9006
[60] Ding Y, Yamada R, Gresback R, Zhou S, Pi X and Nozaki T 2014 A parametric study of non-thermal plasma synthesis of silicon nanoparticles from a chlorinated precursor *J. Phys. D: Appl. Phys.* **47** 485202
[61] Yasar-Inceoglu O, Lopez T, Farshihagro E and Mangolini L 2012 Silicon nanocrystal production through non-thermal plasma synthesis: a comparative study between silicon tetrachloride and silane precursors *Nanotechnology* **23** 255604
[62] Stull D R 1947 Inorganic compounds *Ind. Eng. Chem.* **39** 540–50
[63] Beaudette C A, Held J T, Mkhoyan K A and Kortshagen U R 2020 Nonthermal plasma-enhanced chemical vapor deposition of two-dimensional molybdenum disulfide *ACS Omega* **5** 21853–61
[64] Kannan G and Desikan P 1985 Critical appraisal and review of aluminium chloride electrolysis for the production of aluminium *Bull. Electrochem.* **01** 483–8
[65] Zheng J, Sun B, Yang R, Song X, Li X and Pu Y 2008 Metal Al produced by H_2 plasma reduction of $AlCl_3$: a thermodynamic and kinetic study on the plasma chemistry *J. Phys. Chem.* B **112** 12748–52
[66] Patnaik P 2003 *Handbook of Inorganic Chemicals* vol 529 (New York: McGraw-Hill)
[67] Holder C F and Schaak R E 2019 Tutorial on powder X-ray diffraction for characterizing nanoscale materials *ACS Nano* **13** 7359–65

[68] Rogowski D F, Marshall P and Fontijn A 1989 High-temperature fast-flow reactor kinetics studies of the reactions of aluminum with chlorine, aluminum with hydrogen chloride and aluminum monochloride with chlorine over wide temperature ranges *J. Phys. Chem.* **93** 1118–23
[69] Nickel K G, Riedel R and Petzow G 1989 Thermodynamic and experimental study of high-purity aluminum nitride formation from aluminum chloride by chemical vapor deposition *J. Am. Ceram. Soc.* **72** 1804–10
[70] Sommerer T J 1992 Monte Carlo-fluid model of chlorine atom production in Cl_2, HCl, and CCl_4 radio-frequency discharges for plasma etching *J. Vac. Sci. Technol.* B **10** 2179
[71] Kortshagen U R, Sankaran R M, Pereira R N, Girshick S L, Wu J J and Aydil E S 2016 Nonthermal plasma synthesis of nanocrystals: fundamental principles, materials, and applications *Chem. Rev.* **116** 11061–127
[72] Girshick S L 2020 Particle nucleation and growth in dusty plasmas: On the importance of charged-neutral interactions *J. Vac. Sci. Technol.* A **38** 011001
[73] Sherwood P M A 1998 Introduction to studies of aluminum and its compounds by XPS *Surf. Sci. Spectra* **5** 1–3
[74] Paparazzo E 1986 XPS analysis of iron aluminum oxide systems *Appl. Surf. Sci.* **25** 1–12
[75] Li H, Belkind A, Jansen F and Orban Z 1997 An in situ XPS study of oxygen plasma cleaning of aluminum surfaces *Surf. Coat. Technol.* **92** 171–7
[76] Strohmeier B R 1990 An ESCA method for determining the oxide thickness on aluminum alloys *Surf. Interface Anal.* **15** 51–6
[77] Maleki A, Taherizadeh A, Issa H, Niroumand B, Allafchian A and Ghaei A 2018 Development of a new magnetic aluminum matrix nanocomposite *Ceram. Int.* **44** 15079–85
[78] Khalil O M, Mingareev I, Bonhoff T, El-Sherif A F, Richardson M C and Harith M A 2014 Studying the effect of zeolite inclusion in aluminum alloy on measurement of its surface hardness using laser-induced breakdown spectroscopy technique *Opt. Eng.* **53** 014106
[79] Lei X-f and Ma J-x 2010 Synthesis and electrochemical performance of aluminum based composites *J. Braz. Chem. Soc.* **21** 209–13
[80] Laidani N, Bartali R, Tosi P and Anderle M 2004 Argon-hydrogen rf plasma study for carbon film deposition *J. Phys. D: Appl. Phys.* **37** 2593–606
[81] Bogaerts A 2002 Hydrogen addition to an argon glow discharge: a numerical simulation *J. Anal. At. Spectrom.* **17** 768–79